Electronic Supplementary Information

Design and optimization of cobalt-encapsulating vertical graphene nano-hills for hydrogen evolution reaction

Sanjib Baran Roy,[‡,a] Sahng-Kyoon Jerng,[‡,b] Kamran Akbar,[a] Jae Ho Jeon,[a] Linh Truong,[a] Seung-Hyun Chun,*[,a] Min Jong Noh,[‡c] Juho Lee,[‡c] Yong-Hoon Kim,*[,c]

[a] Department of Physics, Sejong University, Seoul 05006, Korea

[b] Graphene Research Institute, Sejong University, Seoul 05006, Korea

[c] School of Electrical Engineering and Graduate School of Energy, Environment, Water, and Sustainability, Korea Advanced Institute of Science and Technology, Daejeon 34141, Korea

* Corresponding Authors: schun@sejong.ac.kr and y.h.kim@kaist.ac.kr

‡These authors contributed equally.

S1. Cross-sectional HRTEM image and elemental profile by EDS

Figure S1 shows cross-sectional HRTEM image of Co(50s)@VGNH and the corresponding EDS profile at a selected area. A 200 nm-thick Au was deposited on VGNH to avoid charge-related damage during focused ion beam process.

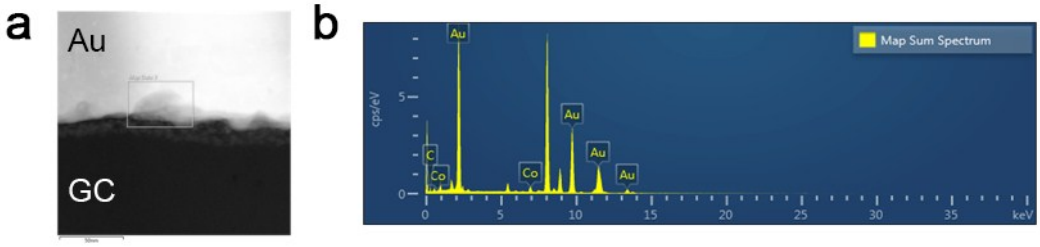

Figure S1. (a) HRTEM image and (b) the corresponding EDS profile. The measured area is marked by the grey box in (a).

S2. Morphology images with EDS mapping for VGNH on different thickness of Co

Figure S2 shows the FESEM images with EDS analysis for (a, c, e) Co(50 s)@ VGNH and (b, d, f) Co(250 s)@VGNH. In contrast to the case of thin Co, thicker Co underneath VGNHs indicates highly segregated Co formation. The relative difference in Co amount is represented in quantitative mapping of elements (e-f). The presence of O can be attributed to oxygen adsorption by VGNHs surface after growth.[1]

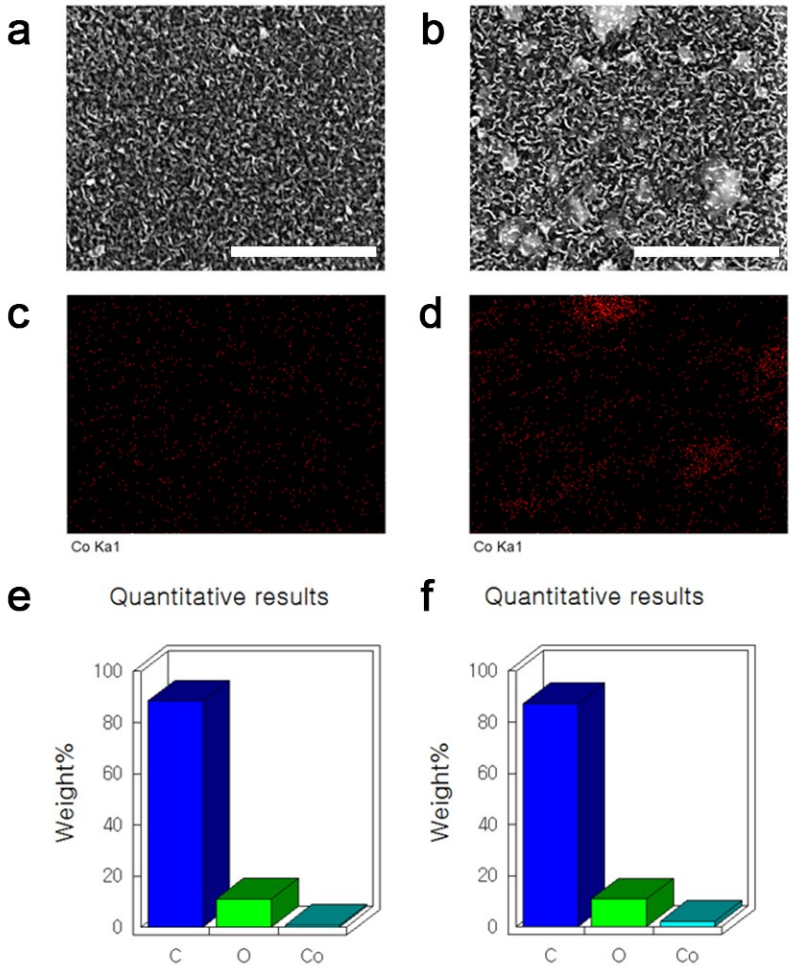

Figure S2. (a-b) Morphology images taken by FESEM, (c-d) elemental mapping by EDS, and (e-f) quantitative results for C, O, Co. Nominally (a, c, e) 1 nm-thick (50 s) and (b, d, f) 5 nm-thick (250 s) Co were used here.

S3. Morphology analysis by AFM

AFM was utilized to investigate the surface morphology. As shown in Figure S3, the roughness of VGNHs increases proportionally as Co thickness increases: (a) bare GC, (b) Co (50 s)@VGNH, (c) Co (100 s)@VGNH, and (d) Co (250 s)@VGNH. When Co is very thin, VGNH consist of small hills and valleys. When thicker Co seed is used for VGNHs, however, the morphology of VGNHs is gradually changed by interconnected hills as huge clusters. The height histograms clearly show the increase of mean height with dispersed height distribution (lower panels of Figure S3). The height of VGNH may depend on the cobalt thickness after optimizing all growth parameters which was previously observed by Yoo *et al*.[2]

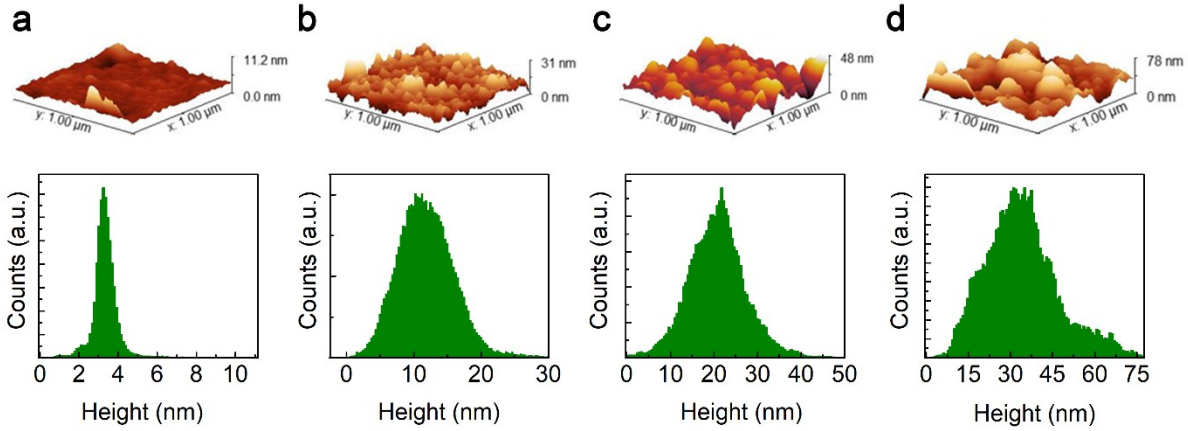

Figure S3. 3D AFM images of (a) bare GC, (b-d) Co (50-250 s)@VGNH (the upper panels), and corresponding relative height histograms (the lower panels).

S4. Co seed dependence of VGNH height

The height histograms of VGNH on various thickness of Co, presented in the Figure S3, were fitted by Gaussian curves. Figure S4 shows the full width half maximum (FWHM) of VGNH from the fitting as a function of Co deposition time. A small value of FWHM indicates that the surface is covered by rather uniform VGNH with small height variations for the thinnest Co seed.

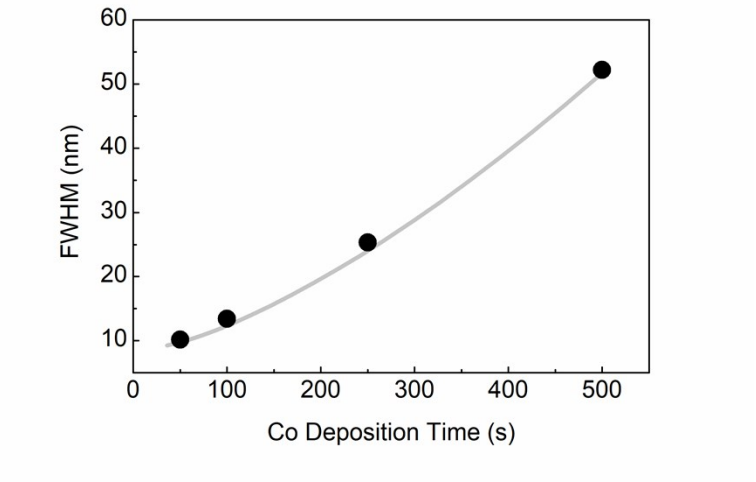

Figure S4. FWHM values of VGNH height distribution as a function of Co deposition time. The grey line is a guide for eyes.

S5. Formation energies of Co*n*@VGNH

Formation energies of Co*n*@VGNH were calculated according to

$$E_{form} = \left[E_{Con@VGNH} - \left(E_{VGNH} + n \times E_{Co,\,vacuum}\right)\right]/n, \qquad (1)$$

where $E_{Con@VGNH}$, E_{VGNH} and $E_{Co,vacuum}$ are total energies of Co*n*@VGNH, bare VGNH and Co atom in vacuum, respectively.

S6. Gibbs free energies for the atomic hydrogen adsorption

To theoretically estimate the HER activity, we calculated the Gibbs free energies for the atomic hydrogen adsorption[3] according to

$$\Delta G_{H^*} = \Delta E_{H^*} + \Delta E_{ZPE} - T\Delta S, \qquad (2)$$

where ΔE_{H^*} is the hydrogen adsorption energy, ΔE_{ZPE} is the zero-point energy (ZPE) difference between the adsorbed and gas-phase hydrogens, and ΔS is the corresponding entropy difference. The hydrogen adsorption energies were calculated according to

$$\Delta E_{H^*} = \left[E_{substrate+H} - \left(E_{substrate} + 1/2E_{H_2}\right)\right], \qquad (3)$$

where $E_{substrate+H}$, $E_{substrate}$ and E_{H_2} are the total energies of the hydrogen-adsorbed substrate, bare substrate, and hydrogen molecule in vacuum, respectively.

In calculating the ZPE of a hydrogen atom adsorbed onto a substrate, we relaxed only the attached hydrogen atom, while fixing all other substrate atoms. This gives only three vibrational frequencies (the degree of freedom of a hydrogen atom), and the averaged ZPE for the Co*n*@VGNH ($1 \leq n \leq 6$) substrate was 0.17 eV, which is in good agreement with that reported for the Co-embedded carbon nanotube cases that have similar local geometry (carbon curvature and underneath Co atoms).[4]

Because the vibrational entropy of an adsorbed hydrogen is negligible, it was calculated according to $\Delta S_H \approx -1/2S^0_{H^2}$, where $S^0_{H^2}$ is the entropy of H_2 in the gas phase at the standard conditions.

Adopting the $T\Delta S$ (at $T = 298.15$ K) value of 0.20 eV according to Ref. 9 amounts to the overall correction value of $\Delta E_{ZPE} - T\Delta S = 0.37$ eV:

$$\Delta G_{H^*} = \Delta E_{H^*} + \Delta E_{ZPE} - T\Delta S = \Delta E_{H^*} + 0.37\ eV \quad . \qquad (4)$$

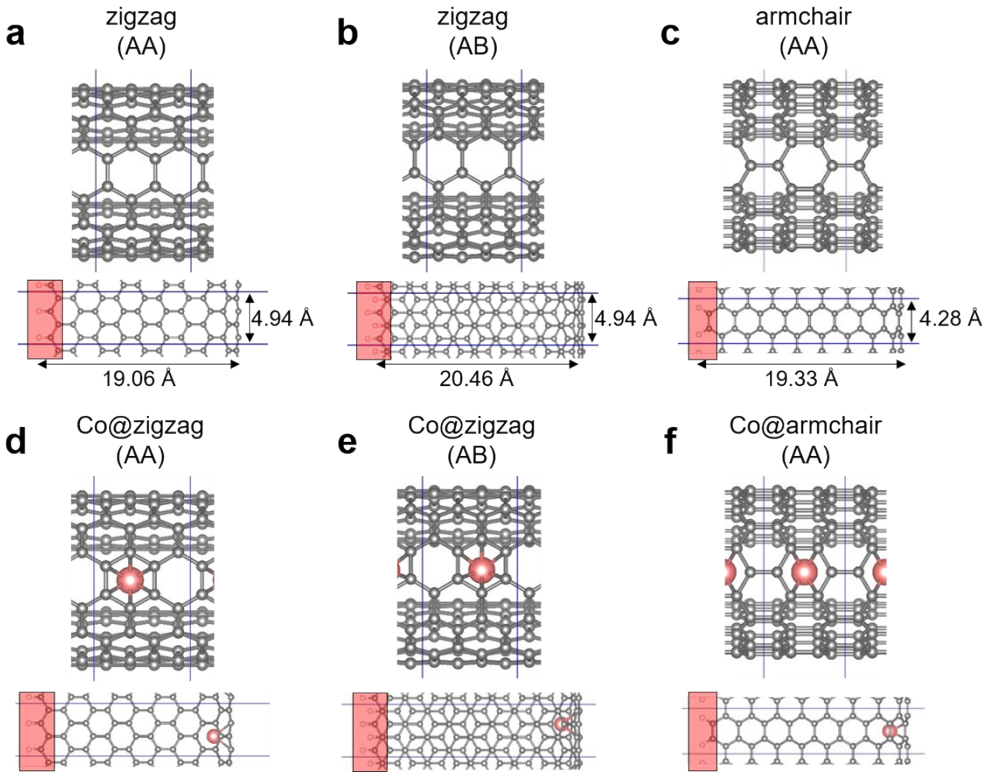

Figure S5. To confirm the general validity of our conclusions, in addition to (a) the VGNH model based on the AA bilayer zigzag graphene edge, we have additionally prepared two other VGNH models based on (b) the AB bilayer zigzag graphene edge and (c) the AA bilayer armchair graphene edge by referring to the folded graphene models available in the literature.[5–7] For the Co1@VGNH models, by referring to the main case based on (d) the AA bilayer zigzag graphene edge (Figure S7), we also prepared two additional models based on (e) the AB bilayer zigzag graphene edge and (f) the AA bilayer armchair graphene edge. In each case, the front (upper) and top (bottom) views are shown together. Considering that the body side of VGNHs do not exactly correspond to the bulk graphite (interlayer distance of 3.35 Å),[8] we fixed the open edge-side interlayer distances of all three models at 3.3 Å for more straightforward comparisons. During geometry optimizations, after passivating the open edge-side dangling bonds by hydrogen atoms, we fixed one last graphene bilayer edge unit cells (shaded area in the top views). The red circles indicate the most favorable hydrogen adsorption sites.

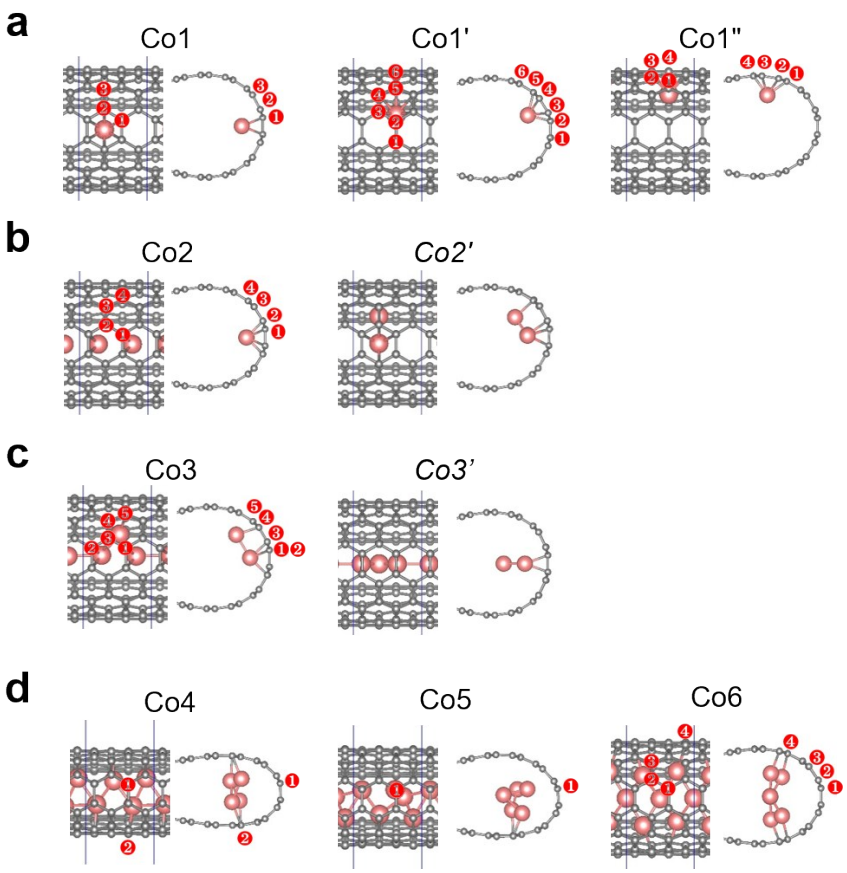

Figure S6. We first carried out DFT geometry optimizations for the Con@VGNH (n = 1 ~ 6) models by starting from several plausible initial Con configurations, and show the front (left) and side (right) views of optimized geometries in each case above (see Table S2 for the corresponding formation energies). (a) Note that for the Co1@VGNH case, we have three energetically comparable geometries (Co1, Co1'. and Co1"; see Table S2). For the (b) Co2@VGNH and (c) Co3@VGNH cases, the energy difference between the optimal and less optimal configurations increased (unfavorable configurations Co2' and Co3' cases are shown on the right), and we did not include them for the atomic hydrogen adsorption calculations. Note that the Co atom(s) are located near the VGNH tip for the Co1 ~ Co3 cases, while they are positioned away from the VGNH tip region in the (d) Co4 ~ Co6 cases. So, we designated the former and latter as the low-density and high-density groups, respectively. The number labels in each model represent the hydrogen adsorption sites with the corresponding adsorption energies given in Table S3.

S7. Electrochemical activity of Co-seeded VGNH and bare Co

Figure S7a shows the HER activity used in the calculation of the onset potential for Co (50 s)@VGNH in the main text. The cyclic voltammetry (CV) of Co (50 s)@VGNH presents the stability during measurements (Figure S7b). Additionally, Figure S7c shows the negligible HER activity of bare Co (50-500 s) on GC electrode, as mentioned in the main text.

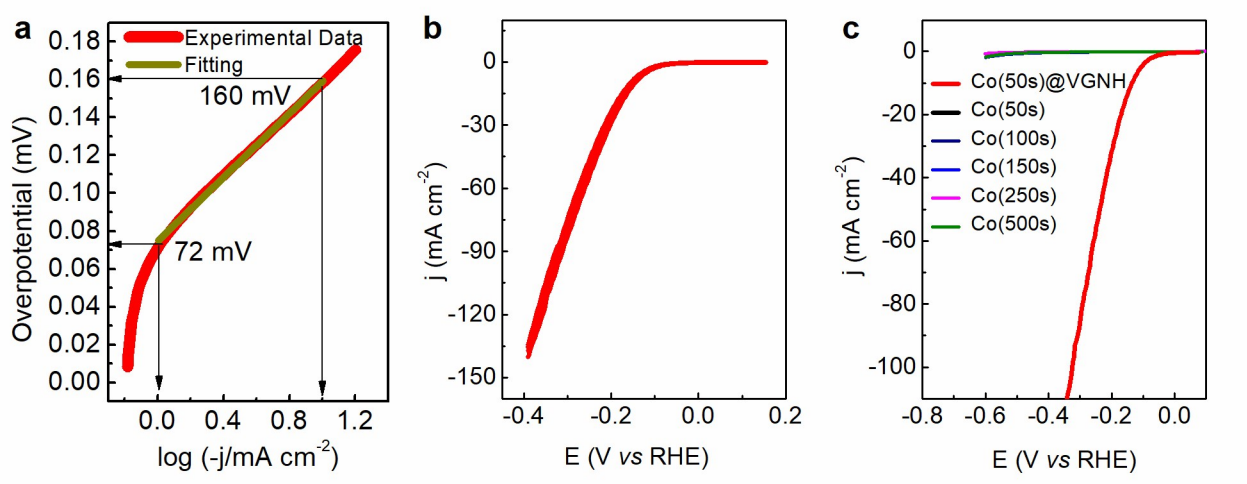

Figure S7. (a) Onset potential obtained from the linear fitting region of Tafel slope (b) the CV of Co (50s)@VGNH. (c) Comparative HER polarization curves of Co (50s)@VGNH and bare Co (50-500 s).

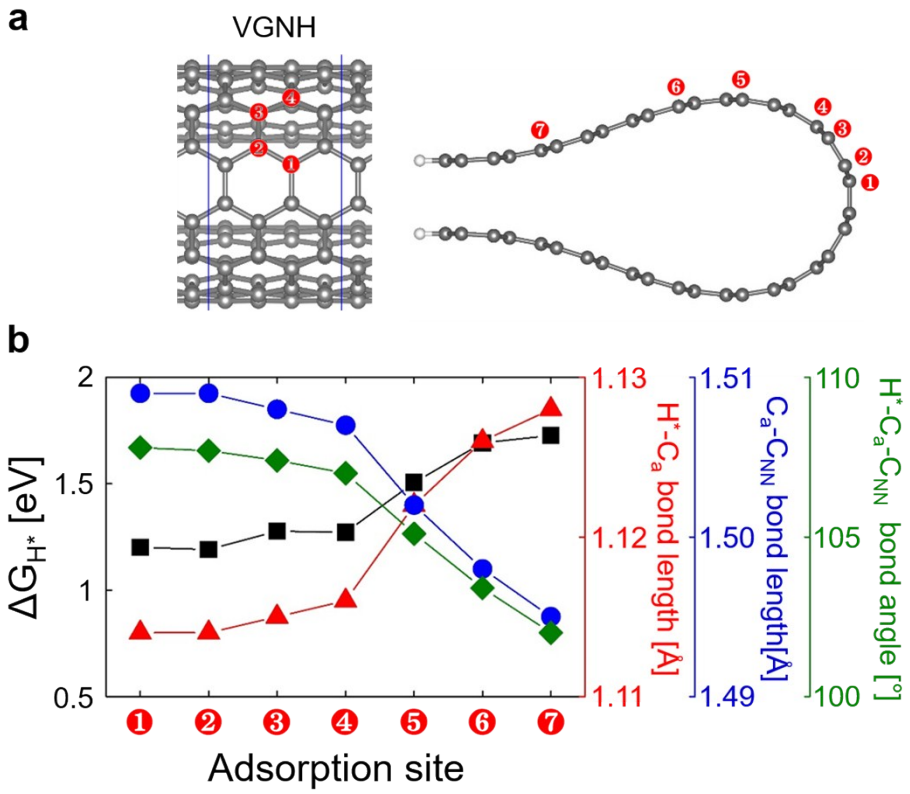

Figure S8. (a) Seven different adsorption sites for the atomic hydrogen adsorption on the bare VGNH model, and (b) the corresponding H* binding geometry and free energy variation trends. Together with the Gibbs free energy ΔG_{H^*} (black square), we show the structural parameters that include the bond length between adsorbed hydrogen H* and active carbon C_a, $d_{H^*-C_a}$ (red triangle), the average bond length between C_a and the three nearest neighbour carbons C_{NN}, $d_{C_a-C_{NN}}$ (blue circle), and the H*-C_a-C_{NN} bond angle, $\theta_{H^*-C_a-C_{NN}}$ (green diamond). Note that, as the H* adsorption site changes from the low curvature (site 7) to the high curvature (site 1) region, we observe the H* adsorption geometry evolving toward the sp^3 bonding type characterized by $d_{H^*-C_a}$= 1.11 Å, $d_{C_a-C_{NN}}$ = 1.51 Å, and $\theta_{H^*-C_a-C_{NN}}$ = 109.0°. Note that in CH_4 the C-H bond length is 1.09 Å and in diamond the C-C bond length is 1.54 Å, and the bond angle is 109.5° In both cases. We can conclude that sp^3-like high C curvature provides more favorable H*-bonding condition.

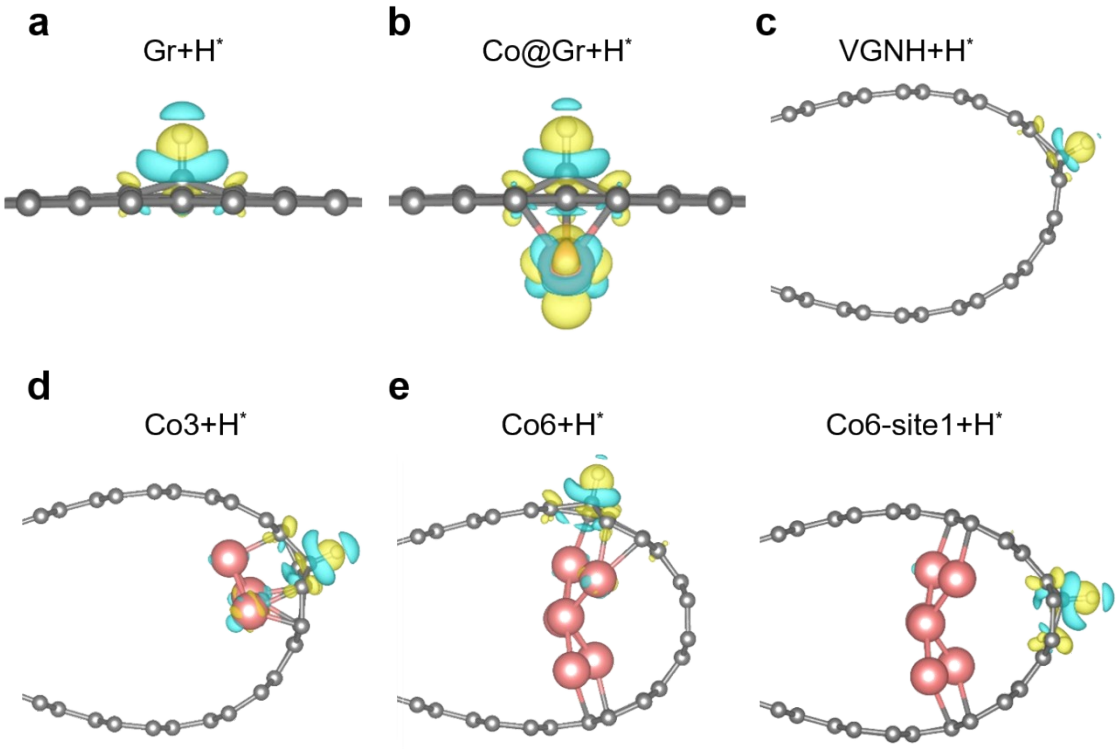

Figure S9. The energetically most favorable H adsorption geometries for the representative (a) bare graphene, (b) Co-embedded graphene (Co@Gr), (c) bare VGNH, (d) Co3@VGNH, and (e) Co6@VGNH cases. For the Co6@VGNH case, we also show a slightly less favorable high-curvature H* adsorption case (Co6-site1). In each case, we overlaid the $\Delta\rho(Con@VGNH - H^*)$ CDD plots, in which the yellow (cyan) colors indicates charge accumulation (depletion) region. The isosurface value is 5×10^{-3} e·Å^{-3}. In all cases, we observe qualitatively similar electron transfer behaviors, with the charge accumulation on the adsorbed hydrogen atom and concurrent charge depletion in the H-graphene/VGNH interface region. In the Co*n*@VGNH cases, we find no direct interactions between Co atoms and adsorbed hydrogen. This trend is different from that of the flat graphene case (Co@Gr), in which we also observe a rather notable charge transfer between graphene and the underneath Co atom due to the reduced distance from graphene to the Co atom (by ~ 0.3 Å compared with the Co*n*@VGNH cases).

Model	ΔE_{H^*} [eV]	ΔG_{H^*} [eV]
zigzag AA VGNH	0.831	1.201
zigzag AB VGNH	0.835	1.205
armchair AA VGNH	0.712	1.082
Co1@zigzag AA VGNH	0.135	0.505
Co1@zigzag AB VGNH	0.217	0.587
Co1@armchair AA VGNH	–0.115	0.255

Table S1. Calculated atomic hydrogen adsorption energies and Gibbs free energies for different VGNH and Co-embedded VGNH models shown in Figure S6. For the pristine VGNH cases, we have obtained essentially identical results irrespective of the AA and AB stacking modes in the "bulk" bilayer graphene regions. The slightly enhanced ΔE_{H^*} for the armchair bilayer graphene-based VGNH can be understood by the slightly reduced relaxation region in the armchair bilayer graphene-based VGNH (compare Figure S6a vs. Figure S6c). For the zigzag bilayer graphene-based Co1@ VGNH cases, we again obtain comparable ΔG_{H^*} values irrespective of the AA and AB stacking of the bilayer region. However, the armchair bilayer graphene-based Co1@VGNH results in a much enhanced ΔE_{H^*} value compared with the zigzag bilayer graphene-based counterparts. This results from different unit cell lengths in the two cases (4.94 Å and 4.28 Å for the zigzag and armchair bilayer graphene, respectively), which effectively increase the Co concentration in the armchair bilayer graphene-based VGNH compared to that in the zigzag bilayer graphene-based VGNH counterpart. We can conclude that adopting different VGNH conformations will not qualitatively modify our conclusions on the HER activity trend.

Model	E_{form} **[eV]**
Co1 / Co1' / Co1"	-2.164 / -2.169 / -2.187
Co2 / *Co2'*	-2.954 / *-2.813*
Co3 / *Co3'*	-3.476 / *-3.385*
Co4	-4.117
Co5	-4.390
Co6	-4.463

Table S2. Calculated formation energies for Con@VGNH models shown in Figure S6. The italicized cases (Co2' and Co3') indicate the energetically unfavorable models compared to their favorable counterparts (Co2 and Co3). For the Co2' and Co3' cases, we did not consider the atomic hydrogen adsorption.

Model	Site	ΔE_{H^*} [eV]	ΔG_{H^*} [eV]
Co1	1	0.199	0.569
	2	**0.135**	**0.505**
	3	0.348	0.718
Co1'	1	0.273	0.643
	2	0.197	0.567
	3	0.166	0.536
	4	0.296	0.666
	5	0.371	0.741
	6	0.478	0.848
Co1"	1	0.548	0.918
	2	0.533	0.903
	3	0.543	0.913
	4	0.718	1.088
Co2	**1**	**-0.020**	**0.350**
	2	0.193	0.563
	3	0.024	0.394
	4	0.568	0.938
Co3	1	-0.251	0.119
	2	-0.264	0.106
	3	**-0.491**	**-0.121**
	4	-0.239	0.131
	5	-0.386	-0.016
Co4	1	0.255	0.625
	2	**0.249**	**0.619**
Co5	**1**	**0.067**	**0.437**
Co6	1	0.536	0.906
	2	0.301	0.671
	3	0.485	0.855
	4	**0.270**	**0.640**

Table S3. The calculated atomic hydrogen adsorption energies and Gibbs free energies for Co*n*@VGNH ($n = 1 \sim 6$) models. The site numbers are as shown in Figure S6. In all cases, the most favorable Gibbs free energy values are indicated in bold face, and they are compiled in Figure 2c left panel. Note that particularly in the low-density Co3@VGNH case most adsorption sites meet the HER activity criterion.

Catalysts	Mass loading (mg/ cm²)	Tafel slope (mV/dec)	Overpotential (vs. RHE) at 10mA /cm²	References
Co-NRCNTs	0.28	69	260 mV	9
FeCo-C	0.285	74	262 mV	10
CoOx@CN	0.12	55	138 mV	11
Mo2C-CNT	2	56	152 mV	12
CoNi@NC	1.6	104	142 mV	13
NG-Mo	0.7	105	140 mV	14
MoP	0.86	54	~150 mV	15
WO3-CNFs	0.21	89	185 mV	16
Ws2-RGO	0.4	58	200 mV	17
Fe2P	-	55	191 mV	18
Co(50s)@VGNHs	***0.0056***	***83***	***160 mV***	***This work***

Table S4. Comparison of HER performance of Co(50s)@VGNHs and other non-noble metal catalysts in acidic media.

References

1 K. Akbar, J. H. Kim, Z. Lee, M. Kim, Y. Yi and S.-H. Chun, *NPG Asia Mater.*, 2017, **9**, e378.

2 M. S. Yoo, H. C. Lee, S. Lee, S. B. Lee, N.-S. Lee and K. Cho, *Adv. Mater.*, 2017, **29**, 1700753.

3 J. K. Nørskov, T. Bligaard, A. Logadottir, J. R. Kitchin, J. G. Chen, S. Pandelov and U. Stimming, *J. Electrochem. Soc.*, 2005, **152**, J23–J26.

4 J. Deng, P. Ren, D. Deng, L. Yu, F. Yang and X. Bao, *Energy Environ. Sci.*, 2014, **7**, 1919–1923.

5 J. Feng, L. Qi, J. Y. Huang and J. Li, *Phys. Rev. B*, 2009, **80**, 165407.

6 N. B. Le and L. M. Woods, *Phys. Rev. B*, 2012, **85**, 035403.

7 W.-J. Yin, Y.-E. Xie, L.-M. Liu, Y.-P. Chen, R.-Z. Wang, X.-L. Wei, J.-X. Zhong and L. Lau, *J. Appl. Phys.*, 2013, **113**, 173506.

8 I. V. Lebedeva, A. A. Knizhnik, A. M. Popov, Y. E. Lozovik and B. V. Potapkin, *Phys. Chem. Chem. Phys.*, 2011, **13**, 5687–5695.

9 X. Zou, X. Huang, A. Goswami, R. Silva, B. R. Sathe, E. Mikmeková and T. Asefa, *Angew. Chemie Int. Ed.*, 2014, **53**, 4372–4376.

10 Y. Yang, Z. Lun, G. Xia, F. Zheng, M. He and Q. Chen, *Energy Environ. Sci.*, 2015, **8**, 3563–3571.

11 Z.-L. Wang, X.-F. Hao, Z. Jiang, X.-P. Sun, D. Xu, J. Wang, H.-X. Zhong, F.-L. Meng and X.-B. Zhang, *J. Am. Chem. Soc.*, 2015, **137**, 15070–15073.

12 W.-F. Chen, C.-H. Wang, K. Sasaki, N. Marinkovic, W. Xu, J. T. Muckerman, Y. Zhu and R. R. Adzic, *Energy Environ. Sci.*, 2013, **6**, 943.

13 J. Deng, P. Ren, D. Deng and X. Bao, *Angew. Chemie Int. Ed.*, 2015, **54**, 2100–2104.

14 S. Chen, J. Duan, Y. Tang, B. Jin and S. Zhang Qiao, *Nano Energy*, 2015, **11**, 11–18.

15 P. Xiao, M. A. Sk, L. Thia, X. Ge, R. J. Lim, J.-Y. Wang, K. H. Lim and X. Wang, *Energy Environ. Sci.*, 2014, **7**, 2624–2629.

16 J. Chen, D. Yu, W. Liao, M. Zheng, L. Xiao, H. Zhu, M. Zhang, M. Du and J. Yao, *ACS Appl. Mater. Interfaces*, 2016, **8**, 18132–18139.

17 J. Yang, D. Voiry, S. J. Ahn, D. Kang, A. Y. Kim, M. Chhowalla and H. S. Shin, *Angew. Chemie Int. Ed.*, 2013, **52**, 13751–13754.

18 C. G. Read, J. F. Callejas, C. F. Holder and R. E. Schaak, *ACS Appl. Mater. Interfaces*, 2016, **8**, 12798–12803.